A Physical Method for Optical Characterization of Pollution in Industrial Wastewater Ponds Using Imaging Spectroscopy

Louis Zaugg, Rodolphe Marion, Malik Chami, Xavier Briottet, and Laure Roupioz

***Abstract*—Investigating the application of remote sensing to water pollution in industrial ponds is of great interest for rapid and cost-effective pollution monitoring. This article presents a method to detect pollutants and map their spatial distribution in industrial ponds using the water inherent optical properties (IOPs), namely the absorption and backscattering coefficients, derived from imaging spectroscopy data. The IOPs of industrial water pollutants remain poorly known. Current remote sensing methods are site-specific and require in situ measurements to calibrate empirically based models. Here, a generic approach is proposed based on the semianalytical radiative transfer model adapted to take into account both the absorption and backscattering coefficients of pollutant particles. The model is then inverted using an alternating multipixel method, named industrial wastewater optical characterization (IWOC), to map the spatial distribution of the pollutants. The performances of IWOC are evaluated using noise-free and noisy simulated datasets for an absorption-dominated water case and a backscattering-dominated water case. The water reflectance spectra (R_{rs}) for noise-free synthetic datasets are satisfactorily retrieved by the IWOC method. The optical properties of the pollutants are also well retrieved, with maximum root mean square error (RMSE) values of 2.43×10^{-3} m^{-1} for the absorption-dominated case and fairly zero for the backscattering-dominated case. A sensitivity study shows that the impact of noise is the highest on the estimates of the spectral slope exponent of the backscattering coefficient. The performances of the IWOC method are also examined through hyperspectral airborne images acquired over relevant study areas. The reflectance R_{rs} is well retrieved with RMSE values ranging from 7.5×10^{-5} sr^{-1} to 5.82×10^{-4} sr^{-1}. The a priori knowledge of the properties of the study areas is consistent with the spatial distribution of the effluents within the ponds as derived from the remote sensing observations. The approach conducted in this article is a first step toward a generic inversion method for the optical characterization of pollution sources in water, which could further lead to an operational method.**

***Index Terms*—Imaging spectroscopy, inversion method, optical characterization, water pollution.**

Manuscript received 14 November 2023; revised 20 January 2024; accepted 19 February 2024. Date of publication 22 February 2024; date of current version 13 March 2024. *(Corresponding author: Rodolphe Marion.)*

Louis Zaugg and Rodolphe Marion are with the CEA/DAM/DIF, F-91297 Arpajon, France (e-mail: louis.zaugg@hotmail.com; rodolphe.marion@cea.fr).

Malik Chami is with the Sorbonne Université Laboratoire Lagrange, Observatoire Côte d'Azur, Université Côte d'Azur, F-06304 Nice, France (e-mail: malik.chami@upmc.fr).

Xavier Briottet and Laure Roupioz are with the ONERA, Université Fédérale de Toulouse, F-31055 Toulouse, France (e-mail: xavier.briottet@onera.fr; laure.roupioz@onera.fr).

Digital Object Identifier 10.1109/JSTARS.2024.3368750

I. Introduction

WATER is a natural resource whose management is subject to political, environmental, and societal debates. With an increasing population living close to coastlines and increasing fresh water needs, water pollution has become a major issue requiring large-scale and rapid monitoring. Although the impact of industrial activities has decreased over the last few decades due to more stringent legislation, they are still one of the major sources of water pollution worldwide [1]. Water is often used in industrial processes for chemical, physical, or mechanical purposes. It may be contaminated with various undesired by-products. It is therefore necessary to treat the effluents before releasing them back into natural water streams. Industrial settling ponds are often used for such treatment [2]. The primary objective of settling ponds is to allow the suspended solids settling at the bottom. Such a process helps minimizing impurities, thus resulting in the production of solid waste. This industrial pollution depends on the type of plant and its effluents [3], which may contain highly hazardous chemicals, including heavy metals or acids, as well as organic and inorganic materials that can harm the ecosystem. The analysis of such water bodies typically relies on in situ experiments, which are often time-consuming and limited in spatial coverage. In this context, remote sensing offers a relevant solution for monitoring water pollution at a large scale.

Imaging spectroscopy has proven to be an efficient technique for optically characterizing water environments within the 400–1000 nm spectral range. Numerous methods have been proposed for analyzing natural waters using spectroscopic data ([4] and references therein). These methods enable the assessment of water quality by monitoring natural components, such as phytoplankton pigments (e.g., chlorophyll-a), colored dissolved organic matter (CDOM), or suspended particulate matter (SPM) concentration both spatially and temporally [5], [6], [7], [8]. The optical properties of open waters dominated by phytoplankton features (commonly known as case-1 water type) are extensively documented ([9] and references therein). Coastal and inland waters, such as rivers or lakes (often referred to as case-2 water type), typically have higher concentrations of CDOM and/or SPM compared to open waters. The monitoring of their quality, which is of primary importance [7], [8], is more challenging due to increased water turbidity and anthropogenic discharges, which make these waters optically more complex than those

found in the open ocean. Typical methods used for analyzing water reflectance include band ratio algorithms [10], [11], reflectance derivatives [12], [13], [14], or quantitative inversion using physical models [15]. Forward models have been proposed to simulate the reflectance for various bio-optical and geometrical configurations using the radiative transfer equation. Examples of such models include hydrolight [16], ocean successive orders with atmosphere advanced [17], and watercolor simulator [18]. These models consider a wide range of bio-optical parameters as inputs, including the inherent optical properties (IOPs), type and size distribution of the water constituents, and the surface roughness of the water. They are robust, however, they require prior knowledge of the absorption, scattering, and backscattering coefficients of hydrosols, which are often nonexistent in severely contaminated water bodies. Semianalytical models typically consist of approximating the radiative transfer equation that leads to the need of a reduced number of input parameters [19]. Finally, empirical models are frequently used for analyzing a specific site using calibration data. Recently, machine-learning methods based on artificial neural network models, both supervised and unsupervised, have been proposed to invert the water reflectance to derive the bio-optical properties of hydrosols [20], [21], [22]. All these techniques are the result of extensive research on natural waters, for which the characterization of optically active components has been widely documented by in situ measurements.

The focus here is on industrial pollutants existing under different forms depending on their size. They are commonly classified as dissolved (<0.2 μm) or suspended (>0.2 μm). Dissolved particles contribute mostly to light absorption, whereas suspended particles contribute mostly to light scattering. Industrial waters may contain a wide variety of chemical elements and their optical properties are seldom known. The use of remote sensing techniques to characterize heavily polluted waters thus remain poorly documented. Only few studies have been conducted on plants, urban effluents, mines, or oil spills (e.g., [23], [24], [25], [26], [27]). Current remote sensing methods used for polluted environments mainly rely on in situ data points and samples to perform linear regression for adjusting an empirical model. Empirical models have been used to detect and map spatial distribution of urban wastewater in rivers [23], rare Earth element (REE) oxides in water [24], or heavy metals in sediment streams [25]. In addition, pollution is often monitored through its impact on natural constituents, such as phytoplankton or CDOM [28]. Empirical models require calibration data or a priori knowledge about the pollutant types and their associated IOPs. Furthermore, semianalytical or analytical models have rarely been adapted for polluted environments to account for the presence of a particular pollutant [29]. However, the lack of IOPs databases dedicated to industrial pollutants makes the use of techniques that are commonly utilized for natural bodies of water (i.e., unpolluted) insufficient.

The objective of this article is to investigate the feasibility of detecting the presence of water pollutants in industrial ponds using their absorption and backscattering coefficients derived from imaging spectroscopy data. Another objective is to analyze their spatial distribution within the ponds. The latter generally contain high concentrations of a reduced number of chemical constituents. On the contrary, natural water bodies may have lower concentrations of pollutants due to dilution and a higher number of constituents. The idea is to propose a method that would be applicable in the future to a wide range of study areas, without requiring prior knowledge on the type of pollutant. The proposed approach, named industrial wastewater optical characterization (IWOC), consists of retrieving a pollutant component and its bio-optical properties (i.e., concentration, absorption, and backscattering coefficients). For that purpose, the pollutant component has been introduced in addition to natural water components into a widely used semianalytical radiative transfer model, hereafter referred to as the "Lee model" [30]. Such an approach focuses on pollutants in the water column excluding nonmiscible materials setting on the water surface (e.g., hydrocarbons and oils).

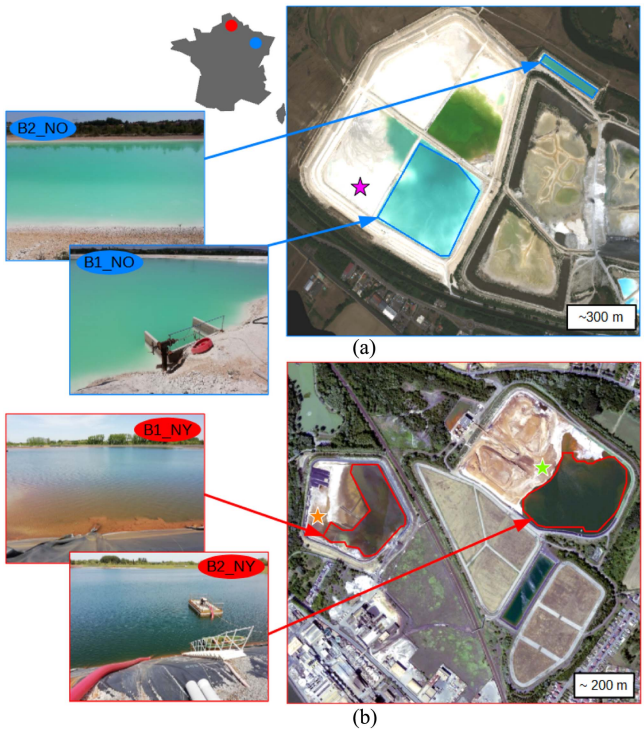

Fig. 1. Airborne hyperspectral images of the study areas with close-up images of the ponds. (a) Novacarb soda ash plant. (b) Nyrstar zinc plant. The stars locate the water-free areas where the bottom reflectances were derived from the images.

The rest of this article is organized as follows. Section II presents the study areas and the hyperspectral images. Section II also provides the theoretical background along with the IWOC methodology and the synthetic datasets used to evaluate it. IWOC is then applied to the synthetic datasets and to the hyperspectral images in Section III. the results are discussed in Section IV. Finally, Section V concludes this article.

II. Material and Method

A. Study Areas and Airborne Hyperspectral Images

1) Study Areas: The first study area is the Novacarb soda ash plant located southward of the city of Nancy (France) [Fig. 1(a)].

TABLE I
CHEMICAL PROPERTIES OF WASTEWATER FROM NOVACARB SITE PONDS (CONCENTRATIONS IN G/L)

	SPM	Chloride	pH
B1_NO	18	105–115	11.0–11.5
B2_NO	<0.05	105–115	–

TABLE II
CHEMICAL PROPERTIES OF WASTEWATER FROM NYRSTAR SITE PONDS (CONCENTRATIONS IN G/L)

	Zn	Mg	Ca	Mn	Cm	SPM	pH
B1_NY	0. 61	0.42	0.42	0.13	0.02	0.01	5.4
B2_NY	10.0	0	0	0	0.45	0	3–4

It produces soda ash using brine and limestone, following the Solvay process [31]. It is characterized by large ponds, a bright blue water color, and a white bottom. Two of these ponds are studied here, referred to as B1-NO and B2-NO. The waters are mainly composed of dissolved salts and suspended matter [32]. Chemical analyses of the ponds were provided by the factory managers (personal communication) and are reported in Table I. For B1-NO, the chloride concentration is in the range 105–115 g/L including 40–45 g/L of Ca^{2+}. Suspended matter mainly consists of coarse particles of sulfates (mainly gypsum) and calcium carbonates. Its concentration is 18 g/L. Water pH is basic with a measured value of 11.0–11.5 for B1-NO. Once a large part of the suspended sulfates has been settled as solids in pond B1-NO, the residual water is transferred to pond B2-NO, prior to discharging into the Meurthe river at a controlled rate. The water in B2-NO is thus mainly composed of dissolved chlorides (the concentration of suspended matter is then less than 50 mg/L), indicating the efficiency of the settling pond protocol.

The second study area is the Nyrstar zinc plant near the city of Douai (North of France) [Fig. 1(b)]. Zinc cathodes are produced following the roast–leach–electrolysis–smelting process [33]. It consists of two large ponds, referred to as B1-NY and B2-NY. These ponds are independent to each other. Public inspection reports indicate that the ponds contain dissolved metals, including zinc, cadmium, or mercury [34]. They also inform on the use of B1-NY to settle muds that leads to the presence of suspended matter. Detailed chemical analyses of the ponds were provided by the factory managers (personal communication) and are reported in Table II. The water in B1-NY has a brownish color and it mainly contains zinc (0.61 g/L), magnesium (0.42 g/L), calcium (0.42 g/L), manganese (0.13 g/L), cadmium (20 mg/L), and some traces of lead. The suspended matter concentration is 10 mg/L. However, its detailed composition remains unknown. The measured pH value is 5.4. The water contained in the pond B2-NY shows a dark greenish color and an ochre area at the northern edge, presumably where the water is discharged from the plant. The main metal components are zinc with a concentration of 10 g/L and cadmium with a concentration of 0.45 g/L. The pH value typically varies between 3 and 4.

2) Airborne Hyperspectral Images: Airborne data were acquired using a Hyspex Mjölnir V-1240 camera within the 400–1000 nm spectral range. The camera is able to provide measurements for 200 bands at 3-nm spectral resolution. The data were collected for a solar zenith angle of approximately 30° in July 2022. Flight lines were oriented from south to north to minimize the sunlight effects. The images were atmospherically corrected using atmospheric and topographic correction (ATCOR) [35] to derive the water surface reflectance. A mid-latitude summer atmospheric model with rural aerosols and a visibility value of 100 km was used. The 820-nm absorption band was selected for water vapor retrieval. The correction was improved using ground reflectance measurements acquired over a bare soil area with an ASD FieldSpec3 HiRes spectroradiometer within the 400–2500-nm spectral range. A spectralon was used as a reference. Then, the measured reflectance was divided by a factor of π to ensure consistency with a remote sensing reflectance quantity (R_{rs}, sr^{-1}). Finally, only the spectral bands between 400 and 700 nm were retained for this article due to the low R_{rs} signal above 700 nm. The native spatial resolution of the airborne images was degraded down to 5 m by averaging to reduce the noise in the data. Regions of interest were created for both study areas to better focus on the ponds (Fig. 1).

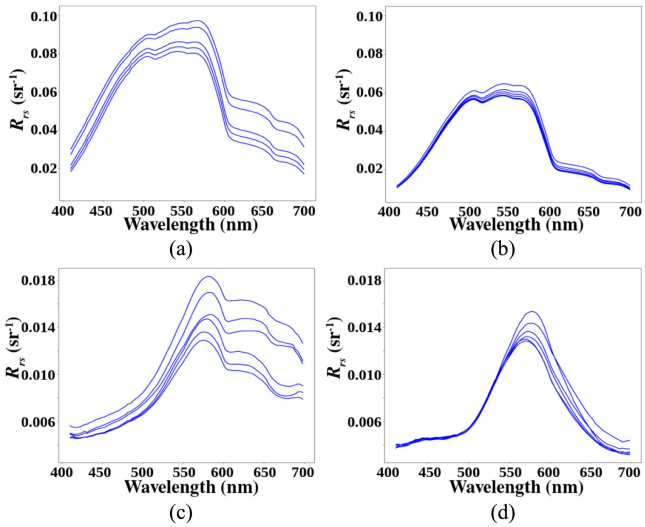

Fig. 2. Some remote sensing reflectances derived from the airborne hyperspectral images. (a) B1-NO and (b) B2-NO, from the Novacarb soda ash plant. (c) B1-NY and (d) B2-NY, from the Nyrstar zinc plant.

Fig. 2(a) and (b) shows some reflectances derived from B1-NO and B2-NO, respectively. The pixels were selected from the shoreline to the center to represent a wide range of reflectances. For clarity, the extraction locations are not indicated on Fig. 1(a) and (b). A greater amplitude and variability of R_{rs} values are observed for B1-NO, which is more turbid than B2-NO. The water-free area where the bottom reflectance of pond B1-NO has been derived is noted using a pink star in Fig. 1(a). Unfortunately, pond B2-NO does not show any water-free area from which the bottom reflectance could be derived. Since both ponds have a similar composition, it is assumed that they have a similar bottom reflectance. The value of the bottom reflectance is fixed in the proposed algorithm (see Section II-C).

Lower R_{rs} amplitudes are observed for B1-NY and B2-NY [Fig. 2(c) and (d)] as a result of the darker features of the ponds. R_{rs} shows multiple shoulders for B1-NY at 600, 650,

and 700 nm, whereas a single peak is observed at 575 nm for B2-NY. Note that a slight spectral shift of the maximum value of R_{rs} to longer wavelengths is observed for B2-NY with increasing turbidity. For both cases, the pond bottom is made of geotextile, a dark surface with a very low reflectance of around 0.05. However, for B1-NY, a brownish mud, which seems to be the settled matter, covers the geotextile. Likewise, for pond B2-NY, goethite, which is the ochre solids piled up beside the pond, covers the geotextile (personal communication). Thus, the bottom reflectance values were derived from the two water-free areas located at the orange star for B1-NY and the green star for B2-NY as shown in Fig. 1(b).

B. Theoretical Background

The forward and inverse Lee models [30] are based on the model proposed by [36]. The forward model uses the IOPs as inputs and provides R_{rs} as output. The total absorption coefficient a is the sum of the individual coefficients of each constituent (1), including pure water a_w, phytoplankton a_{phy}, and CDOM a_{CDOM}. In this article, a pollutant absorption coefficient a_{pol} is introduced to account for their potential absorbing effect as

$$a(\lambda) = a_w(\lambda) + a_{\mathrm{phy}}(\lambda) + a_{\mathrm{CDOM}}(\lambda) + a_{\mathrm{pol}}(\lambda). \quad (1)$$

a_w is well-documented [37], [38]. a_{phy} is defined by the chlorophyll-a absorption signature and is characterized in the Lee model by a parameter P as the main factor for phytoplankton ($P = a_{\mathrm{phy}}(440)$, [39]). The chlorophyll-a absorption coefficient exhibits two distinct peaks: a major peak at 430 nm and a secondary peak at 660 nm. a_{CDOM} shows an exponential decrease with wavelength [40], [41]. The concentration of CDOM is controlled using the parameter G, where $G = a_{\mathrm{CDOM}}(440)$. The unit of both P and G is m^{-1}. Finally, $a_{\mathrm{pol}}(\lambda) = C_{\mathrm{pol}} \times a_{\mathrm{pol}}^{\mathrm{ref}}(\lambda)$, where C_{pol} is a scaling factor used to control the concentration of pollutant between pixels in the same pond (dimensionless) and $a_{\mathrm{pol}}^{\mathrm{ref}}$ represents the "reference" absorption coefficient of the pollutant (m^{-1}).

The total backscattering coefficient b_b is also the sum of the individual coefficients of each constituent (2). Since the suspended matter in the industrial ponds studied here is supposed to be dominated by pollutant particles, the backscattering coefficient may be expressed as

$$b_b(\lambda) = b_{\mathrm{bw}}(\lambda) + b_{bpol}(\lambda) \quad (2)$$

where b_{bw} is the backscattering coefficient of pure water. b_{bw} is determined as half of the value of the pure water scattering coefficient [42]. Considering that in industrial ponds the particulate backscattering is mainly due to the pollutant, b_{bpol} is defined similarly as the backscattering coefficient of suspended particles in the Lee model

$$b_{\mathrm{bpol}}(\lambda) = X\left(\frac{\lambda_0}{\lambda}\right)^Y \quad (3)$$

where $X = b_{\mathrm{bpol}}(\lambda_0)$. The reference wavelength λ_0 is set here to 550 nm. Y is the spectral slope exponent of the backscattering coefficient. Y typically ranges from 0 to 2.5 for natural waters [10], [43].

The extinction, backscattering, scattering, and absorption coefficients are computed using Mie theory [44]. Simulations revealed that the backscattering coefficient may increase with wavelength within a given spectral range for certain coarse particle configurations (e.g., for gypsum particles ranging from 0.01 to 15 μm with a modal radius of 5 μm, see Section II-F and A1). Such a spectral increase is unusual for natural waters. It has also been observed in simulations when the proportion of coarse particles increases (e.g., [45]). The Lee model is modified here to account for the impact of coarse pollutant particles on the spectral shape of the backscattering coefficient by permitting negative values for Y.

The bottom reflectance is expressed as $\rho(\lambda) = B \times \rho_{\mathrm{bottom}}(\lambda)$, where B is a scaling factor and ρ_{bottom} is the spectral shape. Initially, the standard Lee model assumes a bottom that is composed solely of sand [30]. Here, various types of bottom composition that can be encountered for industrial ponds are considered using a ρ_{bottom} spectral shape that is directly derived from the image itself using water-free areas (see Section II-A1).

The Lee model simulates the spectral remote sensing reflectance using the parameters P, G, X, Y, B, and the depth of the water column H. This model also provides an inversion procedure based on optimization algorithms for deriving these parameters from a single reflectance spectrum as input. The introduction into the model of a pollutant with an unknown absorption coefficient leads to an ill-posed problem when attempting to invert the reflectance since the number of variables to be determined is higher than the number of observations. An ill-posed problem implies that several combinations of IOPs could exist for a given pixel from the inversion of a single reflectance. The assumptions formulated in Section II-D will allow to propose a method to minimize this issue.

C. Overview of the Methodology

The proposed IWOC method is based on the modified Lee model version. It is divided into two main parts as shown in the flowchart in Fig. 3. The first part consists in retrieving the IOPs of the hydrosols in the industrial pond by inverting the reflectance. IWOC takes advantage of the simultaneous inversion of several pixels within each pond, which is actually a multipixel inversion, to minimize the ill-posed problem issue. In the second part, the derived IOPs are used to characterize the spatial distribution of a pollutant for each pond.

D. Retrieval of the Optical Properties of the Hydrosols

IWOC is based on two assumptions. The first assumption is that the chemical composition/type of the in-water constituents of a given pond (including the pollutant) is spatially homogeneous. It implies that the pollutant absorption coefficient $a_{\mathrm{pol}}^{\mathrm{ref}}$ is the same for all the pixels of the pond. On the contrary, the concentrations P, G, C_{pol}, and the water column depth H may vary spatially from one pixel to another. Because the backscattering coefficient depends on the distribution of particle size, X and Y can also vary from one pixel to another.

The second assumption is that the bottom composition remains the same over the entire pond area, thus resulting in a

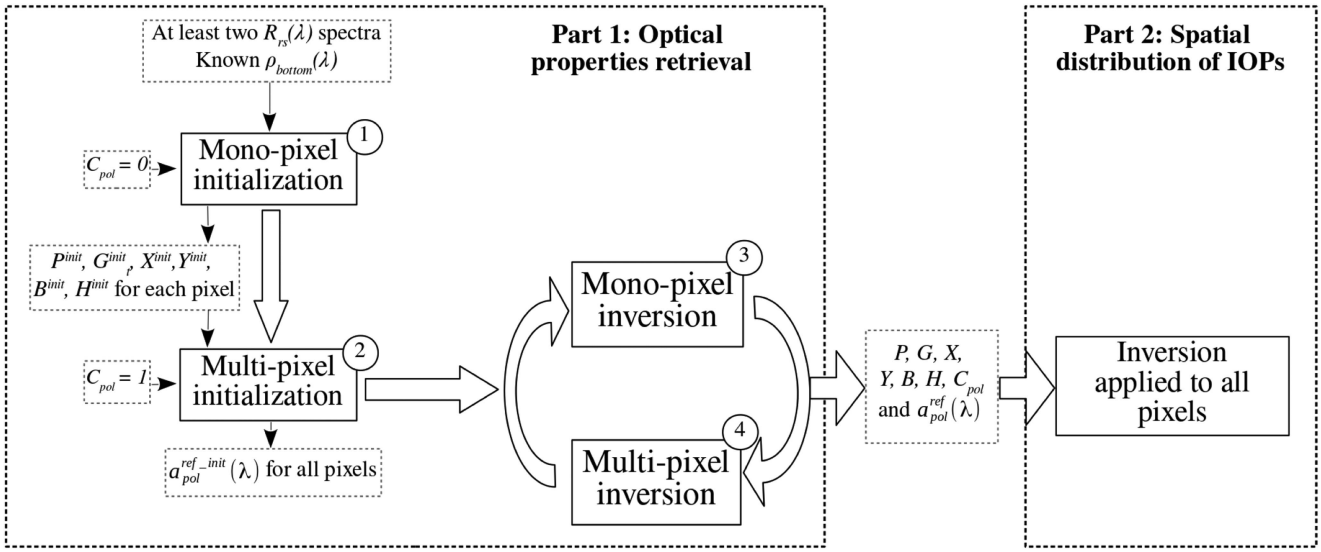

Fig. 3. Flowchart of the IWOC algorithm.

single spectral shape of the bottom reflectance ρ_{bottom} for all pixels. The magnitude of the bottom reflectance is controlled by parameter B which may vary from one pixel to another.

On the basis of these two assumptions, two sets of variables which need to be estimated are identified. The first set of variables comprises elements that spatially vary: $\Phi_{\mathrm{mono}} = \{P, G, X, Y, B, H, C_{\mathrm{pol}}\}$. The second set consists of elements that are similar for all pixels: $\Phi_{\mathrm{multi}} = \{a_{\mathrm{pol}}^{\mathrm{ref}}(\lambda)\}$. The simulated reflectances with Φ_{mono} and Φ_{multi} are compared with measurements by using a local nonlinear least squares fitting approach from a Python implementation package of the "mpfit" algorithm [46]. At least two pixels by pond are used to estimate Φ_{mono} and Φ_{multi}. The reflectance of the selected pixels needs to vary in magnitude (see Section IV). The different steps of the optical properties retrieval process are described below.

1) Monopixel Initialization: In step 1 [Fig. 3], each R_{rs} spectrum undergoes an independent inversion process. This step provides a first determination of P, G, X, Y, B, and H. During this step, C_{pol} is not taken into account since there is no information about $a_{\mathrm{pol}}^{\mathrm{ref}}$ at this stage (i.e., $a_{\mathrm{pol}} = 0$). Therefore, $\Phi_{\mathrm{mono}}^{\mathrm{init}} = \{P^{\mathrm{init}}, G^{\mathrm{init}}, X^{\mathrm{init}}, Y^{\mathrm{init}}, B^{\mathrm{init}}, H^{\mathrm{init}}\}$ and, if m pixels by pond are considered for the inversion process, it becomes

$$\Phi_{\mathrm{mono}}^{\mathrm{init}} = \left\{P_1^{\mathrm{init}}, \ldots, P_m^{\mathrm{init}}, G_1^{\mathrm{init}}, \ldots, G_m^{\mathrm{init}}, X_1^{\mathrm{init}}, \ldots, X_m^{\mathrm{init}}, Y_1^{\mathrm{init}}, \ldots, Y_m^{\mathrm{init}}, B_1^{\mathrm{init}}, \ldots, B_m^{\mathrm{init}}, H_1^{\mathrm{init}}, \ldots, H_m^{\mathrm{init}}\right\}. \quad (4)$$

The monopixel cost function that is minimized is defined by

$$E_{\mathrm{mono}}\left(\Phi_{\mathrm{mono}}\right) = \sum_{i=1}^{n}\left[y_i - F_i^{\mathrm{Lee}}\left(\Phi_{\mathrm{mono}}\right)\right]^2 \quad (5)$$

where i is the band number and n is the number of bands, y is the reflectance measurement, and F^{Lee} is the simulated reflectance from the modified Lee model using the set of parameters Φ_{mono}.

To initialize the minimization at this step, only pure water without any pollutant is considered ($P^{\mathrm{init}} = 0\ \mathrm{m}^{-1}$, $G^{\mathrm{init}} = 0\ \mathrm{m}^{-1}$, $X^{\mathrm{init}} = 0\ \mathrm{m}^{-1}$, $Y^{\mathrm{init}} = 0$, $B^{\mathrm{init}} = 1$, and $H^{\mathrm{init}} = 1$ m). Without a priori knowledge on bio-optical properties of the study area, the variables P, G, X, B, and H are allowed to vary from 0 to 10 (for their respective units). B varies from 0 to the maximum value of $\rho_{\mathrm{bottom}}(\lambda)$, so that the bottom reflectance is between 0 and 1 within the studied wavelength range. Y may vary from -2.5 to 2.5. The negative boundary limit for Y allows accounting for the case where coarse particles exhibit a spectral increase of the backscattering coefficient with wavelength. The upper limit for Y is taken based on [30]. Note that a priori knowledge can already be included at this stage if available, via the initial values and bounds of the parameters.

2) Multipixel Initialization: In step 2 [Fig. 3], the R_{rs} spectra of the m pixels are inverted simultaneously to obtain an estimate of the initial value of $a_{\mathrm{pol}}^{\mathrm{ref}}$, noted $a_{\mathrm{pol}}^{\mathrm{ref\_init}}$, in $\Phi_{\mathrm{multi}}^{\mathrm{init}}$

$$\Phi_{\mathrm{multi}}^{\mathrm{init}} = \left\{a_{\mathrm{pol}}^{\mathrm{ref\_init}}\left(\lambda_1\right), a_{\mathrm{pol}}^{\mathrm{ref\_init}}\left(\lambda_2\right), \ldots, a_{\mathrm{pol}}^{\mathrm{ref\_init}}\left(\lambda_n\right)\right\}. \quad (6)$$

Here, the previously estimated values in $\Phi_{\mathrm{mono\_init}}$ are used as inputs for each corresponding pixel. The multipixel cost function is defined by

$$E_{\mathrm{multi}}\left(\Phi_{\mathrm{multi}}\right) = \sum_{j=1}^{m}\left(\sum_{i=1}^{n}\left[y_{ij} - F_{ij}^{\mathrm{Lee}}\left(\Phi_{\mathrm{multi}}\right)\right]^2\right) \quad (7)$$

where j is the pixel number. The estimates of the first value $a_{\mathrm{pol}}^{\mathrm{ref}}$ of $a_{\mathrm{pol}}^{\mathrm{ref\_init}}$ corresponds to the best fit for the m pixels of the pond since C_{pol} is set to 1 at this stage. To initialize the minimization process, the coefficient $a_{\mathrm{pol}}^{\mathrm{ref\_init}}$ is set to zero for all wavelengths because of the lack of a priori knowledge about the absorption coefficient of any potential pollutants. The boundary limits for $a_{\mathrm{pol}}^{\mathrm{ref}}$ are set between 0 and 10 m^{-1}.

3) Alternating Inversion: Finally, the monopixel and multipixel cost functions are alternatively minimized [47] (steps 3 and 4 in Fig. 3). At each step, the input parameters are the output parameters of the previous step. Step 3 retrieves Φ_{mono} including

C_{pol} (8) using the previously estimated value of $a_{\mathrm{pol}}^{\mathrm{ref}}$ as a fixed parameter and Φ_{mono} as initial values for the inversion

$$\Phi_{\mathrm{mono}} = \{P_1, \ldots, P_m, G_1, \ldots, G_m, X_1, \ldots, X_m, Y_1, \ldots, Y_m, B_1, \ldots, B_m, H_1, \ldots, H_m, C_{pol\,1}, \ldots, C_{\mathrm{pol}_m}\}. \quad (8)$$

Here, the range of variation of C_{pol} is set between 0 and 10. Then, Φ_{mono} derived from step 3 is used in step 4 as fixed parameters and $a_{\mathrm{pol}}^{\mathrm{ref}}$ is used as the initial value for the inversion. Typically, five to ten iterations are required to converge and to derive the optimal set of parameters {*P, G, X, Y, B, H,* C_{pol}, $a_{\mathrm{pol}}^{\mathrm{ref}}$}.

At the end, if the value of $a_{\mathrm{pol}}^{\mathrm{ref}}$ is close or equal to zero, it means that either the water is not polluted or the spectral signature of the pollutant is not highly pronounced. If the value of $a_{\mathrm{pol}}^{\mathrm{ref}}$ significantly differs from zero, it means that the use of the natural constituents only (pure water, phytoplankton, and CDOM) is insufficient to correctly retrieve the IOPs of the pond. Therefore, the presence of an unknown constituent (pollutant) is required to explain the water reflectance spectral signatures. The scale factor C_{pol} is then used to compare the concentration for each pixel. In addition, the observation of an increasing value of the backscattering coefficient with wavelength (i.e., negative *Y* values) suggests the occurrence of a significant proportion of coarse particles that are likely to be pollutants.

E. Mapping of the Spatial Distribution of the IOPs

A procedure is proposed to analyze the spatial distribution of the derived bio-optical properties for each pond. The procedure is based on the monopixel inversion scheme (step 3 in Fig. 3) applied to each pixel of the pond with $a_{\mathrm{pol}}^{\mathrm{ref}}$ set to the value obtained by the IOPs retrieval procedure. The retained $a_{\mathrm{pol}}^{\mathrm{ref}}$ value is that of the pixel which has a C_{pol} value closest to 1 among the *m* pixels used to retrieve the IOPs. By this way, the retrieved map of the spatial distribution of C_{pol} is relative to this reference pixel. The spatial distribution of the other parameters, including natural constituents *P* and *G*, backscattering parameters *X* and *Y*, bottom parameter *B*, and depth *H*, could also be provided by the algorithm. The initialization values at this step are determined by calculating the average of the monopixel parameters estimated for the *m* pixels during the previous alternating inversion. The use of such average contributes to minimize the differences between neighboring pixels and to avoid local minima. The bounds of the parameters are the same as those used for the IOPs retrieval procedure.

F. Synthetic Datasets

Four synthetic datasets were built using the modified Lee model (Section II-B) to evaluate the effectiveness of the IWOC algorithm to retrieve a_{pol} and b_{bpol}. These datasets consist of polluted water cases representing absorption-dominated (dataset #1 and dataset #3) and backscattering-dominated (dataset #2 and dataset #4) scenarios, respectively (Table III). Each dataset contains two R_{RS}, which is the minimum to use IWOC, modeled using the modified Lee model. Dataset #1 is based on existing literature regarding REE oxides in water that exhibit absorption features located at specific wavelengths [25], [48]. A synthetic spectrum of $a_{\mathrm{pol}}^{\mathrm{ref}}$ has been created showing features at 443, 520, and 574 nm [Fig. 4(a)]. Dataset #1 allows to evaluate the relevance of IWOC to identify specific absorption features. Dataset #2 [Fig. 4(b)] consists of a nonabsorbing pollutant that shows an increase of the backscattering coefficient with wavelength. It can be used to evaluate the relevance of IWOC to identify the presence of coarse particles.

Dataset #3 and dataset #4 are generated using more realistic IOPs to evaluate the sensitivity of the IWOC method to model errors. The IOPs are computed using Mie theory for specific types of particles and size distributions (see Section A-1). Dataset #3 [Fig. 4(c)] consists of small hematite particles that are characterized by a size ranging from 0.001 to 0.100

TABLE III
BIO-OPTICAL PARAMETERS USED FOR GENERATING THE SYNTHETIC DATASETS

		P (m^{-1})	G (m^{-1})	X (m^{-1})	Y	B	H (m)	C_{pol}	a_{pol}^{ref} (m^{-1})
Dataset #1	R_{rs} #1	0.0085	0.10	0.03	0.2	0.5	0.8	0.8	REE a_{pol}^{ref}
	R_{rs} #2	0.0120	0.12	0.05	0.2	0.5	1.0	1.0	REE a_{pol}^{ref}
Dataset #2	R_{rs} #1	0.0085	0.10	0.15	−1.0	0.5	0.8	0.8	0
	R_{rs} #2	0.0120	0.12	0.25	−1.0	0.5	1.0	1.0	0
Dataset #3	R_{rs} #1	0.0085	0.10	Hematite b_{bpol}		0.5	0.8	0.8	Hematite a_{pol}^{ref}
	R_{rs} #2	0.0120	0.12	Hematite b_{bpol}		0.5	1.0	1.0	Hematite a_{pol}^{ref}
Dataset #4	R_{rs} #1	0.0085	0.10	Gypsum b_{bpol}		0.5	0.8	0.8	Gypsum a_{pol}^{ref}
	R_{rs} #2	0.0120	0.12	Gypsum b_{bpol}		0.5	1.0	1.0	Gypsum a_{pol}^{ref}

R_{rs} #1 and R_{rs} #2 are the two remote sensing reflectances of each dataset.

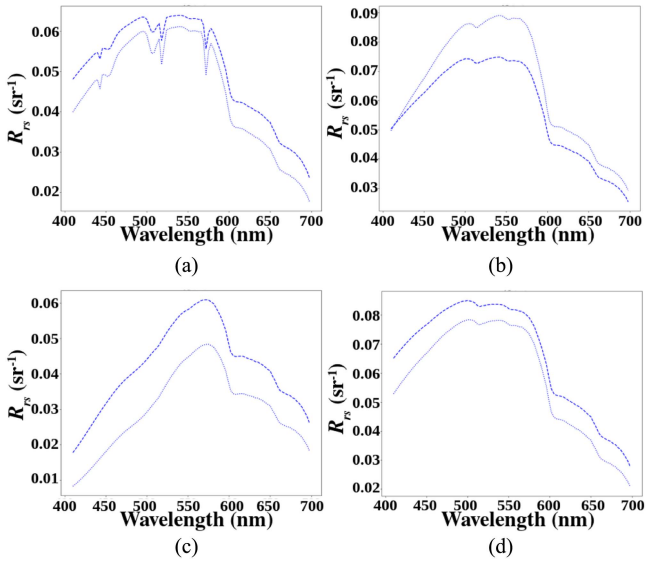

Fig. 4. Synthetic datasets of the remote sensing reflectances generated using the modified Lee model. For each dataset, R_{rs} #1 is the dashed curve and R_{rs} #2 is the dotted curve. (a) Dataset #1. (b) Dataset #2. (c) Dataset #3. (d) Dataset #4.

μm with a modal radius of 0.010 μm. Hematite is selected here to imitate the optical properties of the suspended matter in the Nyrstar ponds, such as goethite (see [49] for a discussion on this point). The absorption coefficient has nonzero values on all the spectral range (unlike dataset #1 which corresponds to absorption features located at specific wavelengths). The backscattering coefficient is well represented by a power law decreasing with wavelength.

Dataset #4 [Fig. 4(d)] consists of coarse gypsum particles that are characterized by a size ranging from 0.01 to 15.00 μm with a modal radius of 5.00 μm. Gypsum is selected here to represent the suspended matter in the Novacarb ponds. b_{bpol} does not follow exactly a power law and is also characterized by an increase with wavelength. Spectral refractive indices for hematite and gypsum were taken from [50] and [51], respectively.

III. Results

In this section, the evaluation of the performances of the IWOC algorithm on the synthetic datasets is outlined. IWOC is then applied to the hyperspectral images acquired over the study areas presented in Section II-A. Note that, due to the low reflectance signal beyond 700 nm, the performances are examined in the spectral range 400–700 nm.

A. Application of IWOC on Synthetic Datasets

1) Relevance of IWOC to Retrieve IOPs: The IWOC method is first applied to dataset #1 (i.e., absorption-dominated scenario). The remote sensing reflectance is satisfactorily fitted with a root mean square error (RMSE) value of 2.0×10^{-6} sr^{-1} [Fig. 5(a)].

The absorption coefficient of the pollutant a_{pol} is retrieved with an RMSE value of 6.4×10^{-4} m^{-1} [Fig. 5(b)]. In particular, the absorption features of REE at 443, 520, and 574 nm are distinctly observable. Slight overestimations of a_{pol} are observed near 400 nm and from 600 to 700 nm. The magnitude of b_{bpol} is satisfactorily determined with an RMSE value of 1.6×10^{-3} m^{-1} [Fig. 5(c)], even in the presence of a small error in the slope value Y. The errors for the retrieved IOPs may be caused by the monopixel initialization step, which does not consider $a_{\mathrm{pol}}^{\mathrm{ref}}$. As a result, the absorption and backscattering coefficients of natural constituents may compensate the lack of pollutant absorption features. The application of IWOC to dataset #1 illustrates its relevance to retrieve the IOPs in this absorbing scenario.

The IWOC method is then applied to dataset #2 (i.e., backscattering-dominated scenario). The retrieved remote sensing reflectance fits very well with the expected values with an RMSE close to 0 [Fig. 5(d)]. The absorption coefficient of the pollutant $a_{\mathrm{pol}}^{\mathrm{ref}}$ is estimated to be zero with insignificant numerical oscillations of the order of 1×10^{-16} m^{-1} [Fig. 5(e)]. The backscattering coefficient b_{bpol}, which is characterized by an increase with wavelength (i.e., Y is negative), is retrieved with an RMSE equal to 0 [Fig. 5(f)]. The application of IWOC to dataset #2 demonstrates the successful retrieval of IOPs in this purely scattering scenario. Dataset #2 shows a higher retrieval accuracy compared to dataset #1 due to the fact that $a_{\mathrm{pol}}^{\mathrm{ref}}$ is not estimated during the monopixel initialization. In contrast, dataset #2 takes into account all the IOPs (including the pollutant component b_{bpol}) during the initialization step, thus leading to their more accurate overall retrieval. The use of synthetic datasets highlights the excellent retrieval of the reflectance spectra and satisfactory estimations of the IOPs (with weak RMSE values). The evaluation of the performances of IWOC also reveals potential errors that might occur when applying the technique to specific cases, particularly for significant magnitudes of a_{pol} with absorption peaks at specific wavelength, like for dataset #1.

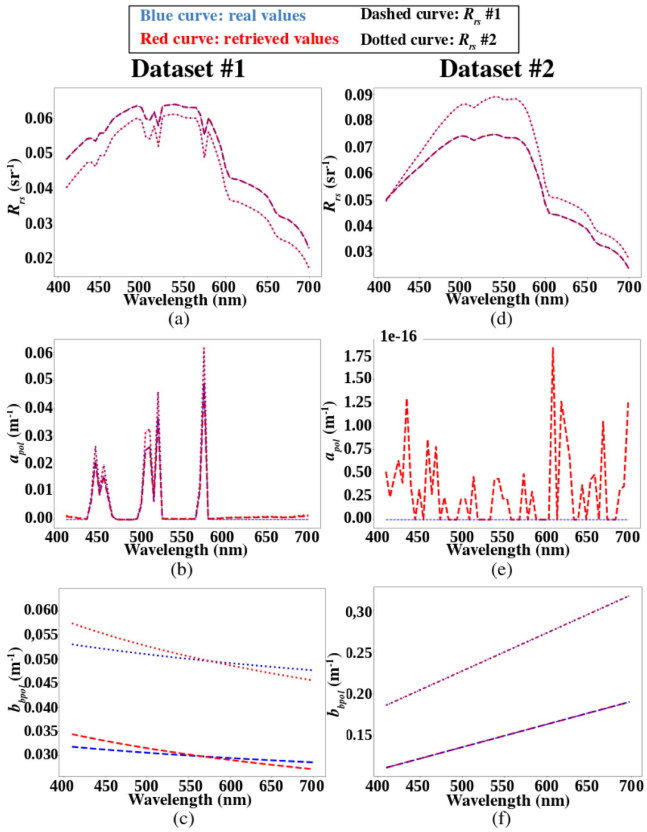

Fig. 5. Retrieval of R_{rs} and IOPs from the IWOC algorithm applied to synthetic dataset #1 and dataset #2. (a) Spectral reflectance for the absorption-dominated case. (b) Absorption coefficient for the absorption-dominated case. (c) Backscattering coefficient for the absorption-dominated case. (d), (e), and (f) are similar to (a), (b), and (c) but for the backscattering-dominated case.

2) Sensitivity of IWOC to Model Errors: Datasets using more complex spectral shapes are used to examine the sensitivity of IWOC to model errors, namely dataset #3 (hematite) and dataset #4 (gypsum). The remote sensing reflectance is accurately retrieved for the hematite case with an RMSE value of 1.68×10^{-4} sr^{-1} [Fig. 6(a)]. Hematite particles have an absorption coefficient that has nonzero values for all the studied spectral range (i.e., no feature at specific wavelength). The spectral shape of $a_{\mathrm{pol}}^{\mathrm{ref}}$ is close to that of a_{CDOM}, as shown by the blue curves in Fig. 6(b). Since $a_{\mathrm{pol}}^{\mathrm{ref}}$ is not estimated during the monopixel initialization step, a_{CDOM} somehow compensates for the lack of $a_{\mathrm{pol}}^{\mathrm{ref}}$ at this step. Comparison between real and estimated values of the sum $a_{\mathrm{pol}} + a_{\mathrm{CDOM}}$ confirms that CDOM properties may compensate for the absence of pollutant as mentioned above

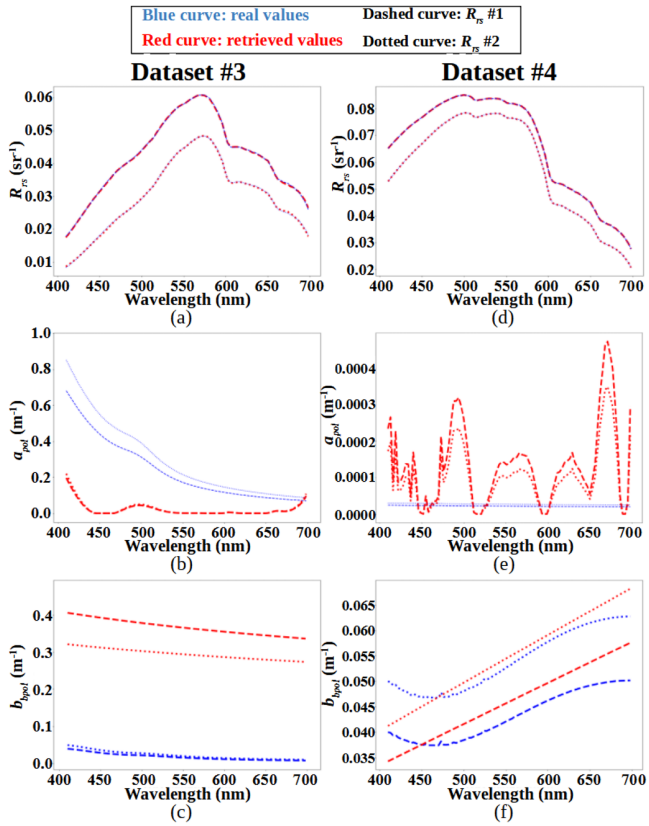

Fig. 6. Retrieval of R_{rs} and IOPs from the IWOC algorithm applied to synthetic dataset #3 and dataset #4. (a) Spectral reflectance for the hematite case. (b) Absorption coefficient for the hematite case. (c) Backscattering coefficient for the hematite case. (d), (e), and (f) are similar to (a), (b), and (c) but for the gypsum case.

(see subsection A-2, Fig. 13). The similarity between a_{pol} and a_{CDOM} spectral shapes leads to an overestimation of G during the monopixel initialization, and then to an underestimation of a_{pol} during the multipixel initialization. The spectral slope of $a_{\mathrm{pol}}^{\mathrm{ref}}$ is not well determined here, but the steeper part near 400 nm as well as the absorption feature from 460 to 520 nm are correctly retrieved [Fig. 6(b)]. The fact that G is overestimated during the monopixel initialization also impacts the retrieval of b_{bpol}, which is initialized at the same step [Fig. 6(c)].

R_{rs} is accurately retrieved by IWOC for dataset #4 with an RMSE value of 3.0×10^{-6} sr^{-1} [Fig. 6(d)]. The retrieved $a_{\mathrm{pol}}^{\mathrm{ref}}$ exhibits values around 1.0×10^{-4} m^{-1}, which are not significant. Thus, the method does not produce false positive values for the absorption. The magnitude of b_{bpol} is correctly retrieved with an RMSE value of 3.4×10^{-3} m^{-1} [Fig. 6(f)]. The small observed differences are due to the fact that the backscattering coefficient of gypsum does not follow the power law used in the Lee model (3). However, the power law is sufficient here to characterize the backscattering (magnitude and presence of coarse particles).

3) Sensitivity of IWOC to Noise in the Measurements: The sensitivity of the IWOC algorithm to noise in the measurements is examined by adding to dataset #1 and dataset #2 a zero-mean, additive Gaussian noise with a wavelength-independent standard deviation. Three values are selected, namely $\sigma_{\mathrm{noise1}} = 0.001$ sr^{-1}, $\sigma_{\mathrm{noise2}} = 0.002$ sr^{-1}, and $\sigma_{\mathrm{noise3}} = 0.003$ sr^{-1}. These values are consistent with a range of signal-to-noise ratios of 60, 30, and 20, respectively, considering a mean reflectance signal of 0.06 sr^{-1} for dataset #1 and dataset #2.

TABLE IV
SENSITIVITY OF IWOC TO A LOW NOISE (σ_{NOISE1})

Dataset number	Error on:	MAPE (%)							RRMSE (%)	
		P	G	X	Y	B	H	C_{pol}	b_{bpol}	a_{pol}
#1	R_{rs} #1	68.6	6.6	36.5	835.6	0.7	4.6	32.6	7.3	11.0
	R_{rs} #2	89.7	8.0	30.0	638.2	1.7	4.1	26.5	5.4	10.3
#2	R_{rs} #1	89.6	20.1	35.2	85.1	11.9	8.0	185.5	5.3	0.2
	R_{rs} #2	44.2	12.3	22.4	58.8	40.4	8.6	84.4	4.3	0.1

The mean absolute percentage error (MAPE) is used to quantify the differences between the retrieved and the real scalar parameters as

$$\mathrm{MAPE} = \left| \frac{y^{\mathrm{real}} - y^{\mathrm{retrieved}}}{y^{\mathrm{real}}} \right| \times 100 \tag{9}$$

with y^{real} the real value and $y^{\mathrm{retrieved}}$ the retrieved value. The relative RMSE (RRMSE) is used to quantify the differences between the retrieved and the real vector parameters b_{bpol} and a_{pol} as

$$\mathrm{RRMSE} = \sqrt{\frac{1}{n}\sum_{i=1}^{n} \frac{\left(y_i^{\mathrm{real}} - y_i^{\mathrm{retrieved}}\right)^2}{\left(y_i^{\mathrm{real}}\right)^2}} \times 100. \tag{10}$$

For each dataset and each noise level, 50 random samples are generated on which IWOC is applied. The average and standard deviation of the errors are calculated. The resulting average errors are reported in Table IV for σ_{noise1}. It should be highlighted here that the errors on a_{pol} are meaningful, whereas the errors on C_{pol} are not, since it is a relative scaling factor. Moreover, the RRMSE values for dataset #2 are equivalent to the mean of the estimated a_{pol} as the y^{real} values are set to zero.

P shows high MAPE values (>44%), with slightly higher errors for the absorption-dominated scenario (dataset #1). MAPE is calculated based on a division by the input value, so high MAPE values may be artificially due to the low input values for P (see Table III for input values). G shows acceptable MAPE values ranging from 6% to 8% for dataset #1 and from 12% to 20% for dataset #2. The highest error is observed for the estimation of the backscattering coefficient b_{bpol} (parameter X) especially for the absorption-dominated scenario (dataset #1). The estimation of Y is much more sensitive to noise than that of X. Here, X shows an average MAPE value of 30% when Y MAPE values range from 638% to 835% for dataset #1. The mean standard deviation of Y is 1.05, which is relatively high compared to the range of variation of Y. The significantly higher MAPE for Y that is observed in dataset #1 could be ascribed to the monopixel initialization step, which does not take into account the occurrence of a_{pol}, as highlighted in Section II-B. Therefore, the algorithm attempts to compensate the pollutant absorption

TABLE V
SENSITIVITY OF IWOC TO A HIGHER NOISE (σ_{NOISE2} AND σ_{NOISE3})

	MAPE (%)							RRMSE (%)	
	P	G	X	Y	B	H	C_{pol}	b_{bpol}	a_{pol}
Dataset #1 σ_{noise2}	127.1	18.2	81.4	1083.4	3.4	8.2	60.6	10.3	16.7
Dataset #1 σ_{noise3}	177.8	32.7	157.8	1045.7	6.8	14.2	97.0	22.1	35.4
Dataset #2 σ_{noise2}	81.5	31.7	40.9	96.0	40.2	12.6	144.2	6.7	0.3
Dataset #2 σ_{noise3}	113.4	46.9	48.1	101.8	41.8	14.7	142.0	9.7	0.4

coefficient that is ignored as well as the noise in the dataset which induces a decrease of the performance of the algorithm. In addition, it is likely that the minimization process may encounter a local minima. *B* MAPE values are higher for dataset #2, which is consistent because *B* and the backscattering coefficient b_{bpol} both affect the overall magnitude of R_{rs} and therefore may compensate each other. *H* is satisfactorily retrieved despite the noise in the datasets for both cases, with an MAPE value of 4% for dataset #1 and 8% for dataset #2. RRMSE values are higher for b_{bpol} and a_{pol} for dataset #1, which highlight the high sensitivity to noise of IWOC when working with absorbing pollutants. Furthermore, RRMSE values are within an acceptable range for dataset #1 and dataset #2.

Table V presents MAPE and RRMSE values averaged for R_{rs} #1 and R_{rs} #2 for both datasets for σ_{noise2} and σ_{noise3}. It is observed that most of the errors increase with noise, especially MAPE values for parameter *Y*, which are highly significant for dataset #1 (>1045%). For dataset #2, MAPE values do not significantly increase for *Y*. The retrieval of *B* and *H* remains globally satisfactory considering the high noise level, except for *B* for dataset #2. The difference in the MAPE values for *B* for dataset #1 and dataset #2 may be attributed to the similarity of the influence of the backscattering coefficient and the bottom reflectance on the water surface reflectance, as discussed previously. RRMSE values increase with noise for dataset #1. The retrieval of b_{bpol} and a_{pol} remains satisfactory for σ_{noise2}, whereas RRMSE values for σ_{noise3} are highly degraded with values above 20%. RRMSE values in dataset #2 for b_{bpol} increase with noise but still remain below 10%. The same is observed for a_{pol}. Here, a_{pol} seems to increase with noise despite the real value is zero.

B. Novacarb Soda Ash Plant

1) Retrieval of the IOPs From IWOC Algorithm: The application of IWOC to retrieve the IOPs requires at least two pixels. The minimum and maximum R_{rs} were therefore selected from each dataset B1-NO and B2-NO (Section II-A2). The IWOC algorithm leads to a highly satisfactory retrieval of the reflectance for both ponds with RMSE values of 2.1×10^{-4} sr^{-1} and 5.1×10^{-5} sr^{-1} for B1-NO and B2-NO, respectively [Fig. 7(a) and (b)]. The retrieved pollutant absorption coefficient $a_{\mathrm{pol}}^{\mathrm{ref}}$ shows similarities for both ponds [Fig. 7(c) and (d)]. $a_{\mathrm{pol}}^{\mathrm{ref}}$ decreases from 400 to 450 nm. Its magnitude is slightly higher for B2-NO than for B1-NO. The increase of $a_{\mathrm{pol}}^{\mathrm{ref}}$ from 650 to

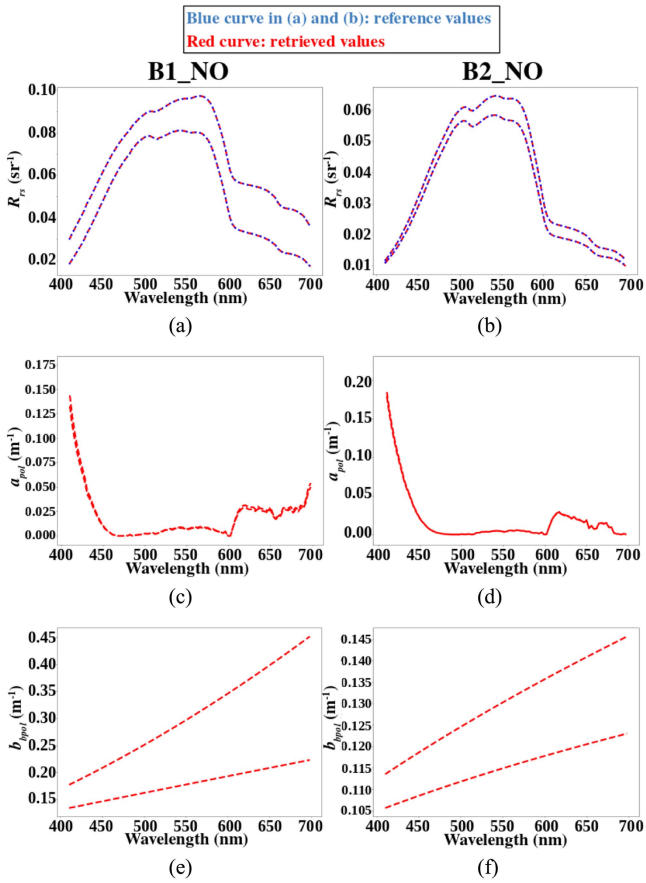

Fig. 7. R_{rs} and IOPs retrieved with IWOC algorithm applied to the airborne image of the soda ash plant. (a) and (b) Spectral reflectance for B1-NO and B2-NO, respectively. (c) and (d) Absorption coefficient of the pollutant for B1-NO and B2-NO, respectively. (e) and (f) Backscattering coefficient of the pollutant for B1-NO and B2-NO, respectively.

700 nm that is observed for B1-NO is not observed for B2-NO. The similarities observed for a_{pol} between B1-NO and B2-NO may be attributed to the similarities in the composition of the dissolved particles. For both cases, the retrieved backscattering coefficient of the pollutant increases with wavelength [Fig. 7(e) and (f)]. Such a spectral shape is consistent with the fact that the suspended matter consists of coarse particles of sulfates. Mie calculations for this case support a spectral increase of b_{bpol} for coarse particles, such as hydrosols composed of gypsum (Section II-B). The magnitude of the retrieved b_{bpol} is consistent with the occurrence of a higher amount of suspended particles for B1-NO than for B2-NO. Estimating a two times lower b_{bpol} for B2-NO highlight the effectiveness of the settling procedure.

2) Spatial Distribution of the Retrieved Parameters: The spatial distribution of the parameters C_{pol}, *H*, *X*, and *Y* derived from the monopixel inversion are shown in Fig. 8. The settling pond B1-NO, where the water is released, is first examined for the soda ash plant. The spatial distribution of C_{pol} is fairly uniform with lower values at the edges of the pond, as corroborated by a prevalence of bright pixels [Fig. 8(a)]. The mean value of C_{pol} is 1.53 with a standard deviation of 0.27. An area with higher C_{pol} values is observed at the center of the pond.

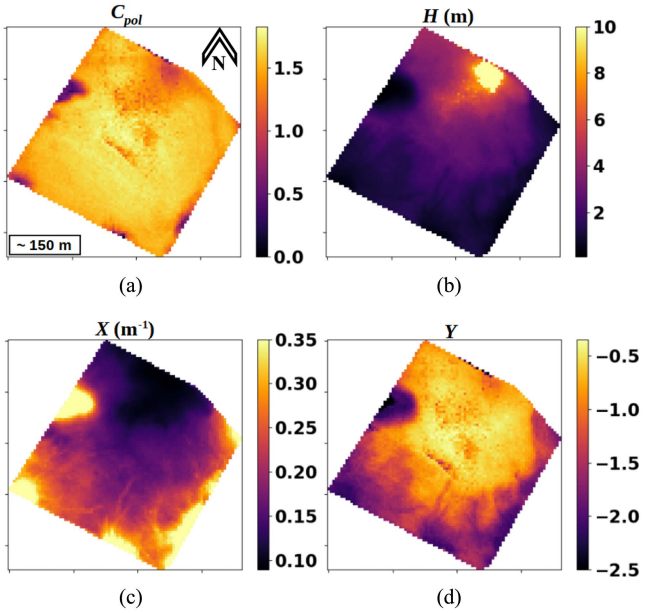

Fig. 8. Spatial distribution of retrieved IOPs parameters for pond B1-NO using the monopixel inversion. (a) C_{pol}, (b) H (m), (c) X (m^{-1}), and (d) Y.

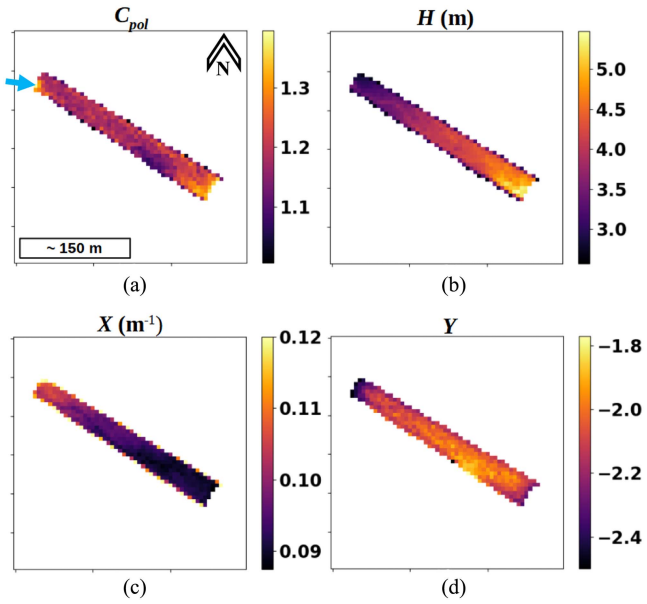

Fig. 9. Spatial distribution of retrieved IOPs parameters for pond B2-NO using the monopixel inversion. (a) C_{pol}, (b) H(m), (c) X(m^{-1}), and (d) Y. Blue arrow is the known discharge location.

The spatial variation of the pond depth H is in agreement with the observation made on the color images [Fig. 1(a)], where the northeast part of the pond is the deepest [Fig. 8(b)]. The mean H value is 2.5 m. The retrieval of H spatial distribution is consistent with airborne observed features. However, errors in the estimated depth values may occur due to high turbidity of the water in the pond (mean X value is 0.21 m^{-1}). X values are higher close to the shorelines of the pond [Fig. 8(c)]. The bright areas surrounding the ponds show the areas where the water is particularly shallow, yielding a high magnitude of R_{rs} and consequently high values of b_{bpol} estimates.

X values decrease away from the source of effluent discharge, which could be also attributed to the settling of the largest suspended matter in the primary pond that leads to moderately coarse particles behind. The spatial variation of X shows linear features from the southern edge of the pond to its center. Such a spatial variation could highlight the direction of water displacement, moving from brighter spots toward deeper areas. It could be due as well to residual flowing water channels when the pond is less full. The spatial variation of the backscattering spectral slope Y also shows similar features (residual flowing water channels) as for X with lower values in the same areas [Fig. 8(d)]. The spectral slope of b_{bpol} is lower than that of the deepest part of the pond. Note that its value remains systematically negative.

The only effluent discharge location in pond B2-NO is pointed by the blue arrow in Fig. 9(a). C_{pol} values range from about 1 to 1.4 with higher values noted at the upper left and lower right edges, with an average value of 1.19 [Fig. 9(a)]. A slight decrease in C_{pol} values is observed along the southern edge of the pond. The depth of the pond is shallower near the water's release area (2.5 m) and it increases along the pond to reach 5.5 m [Fig. 9(b)]. The retrieved mean depth of this pond is 3.9 m. The backscattering coefficient of the pollutant is lower than that of B1-NO. It is possible that the milky aspect of the water leads to an error in the estimation of the depth values. As shown in Fig. 9(c), X values are in agreement with expectations, showing higher values at the northwest part where the water is released, and reaching up to 0.12 m^{-1}. X subsequently decreases to reach a minimum value at the southeast corner of the pond (0.09 m^{-1}). The mean value for X is 0.098 m^{-1}, which is much lower than that of B1-NO (0.21 m^{-1}). Finally, the spatial variations in Y are opposed to those observed for C_{pol} with lowest values at the western and eastern edges of the pond and the highest values along its southern border [Fig. 9(d)].

C. Nyrstar Zinc Plant Ponds

1) Retrieval of the IOPs From IWOC Algorithm: The minimum and maximum R_{rs} were selected from each dataset B1-NY and B2-NY (Section II-A2). The inversion of the reflectance from the IWOC algorithm provides satisfactory retrievals of R_{rs} with RMSE values of 7.2×10^{-5} sr^{-1} for B1-NY and 6.1×10^{-5} sr^{-1} for B2-NY [Fig. 10(a) and (b)]. Weak differences between measured and retrieved values of R_{rs} are observed for B1-NY, particularly around 600 nm [Fig. 10(a)]. The retrieved absorption coefficient of the pollutant shows the same features for both ponds. The main spectral signatures of $a_{\mathrm{pol}}^{\mathrm{ref}}$ are observed from 450 to 540 nm, 560 to 600 nm, 610 to 660 nm, and just below 700 nm. The retrieved absorption coefficient reaches 0.04 and 0.25 m^{-1} for B1-NY and B2-NY, respectively. Thus, B2-NY shows higher absorption values [Fig. 10(c) and (d)]. Such a difference could suggest higher amounts of pollutants in the second pond, which is consistent since the latter contains about 10 times more dissolved metal than that of the first pond (Section II-A). Retrievals of the backscattering coefficient differ for the two ponds. B1-NY pond shows an increase of the backscattering

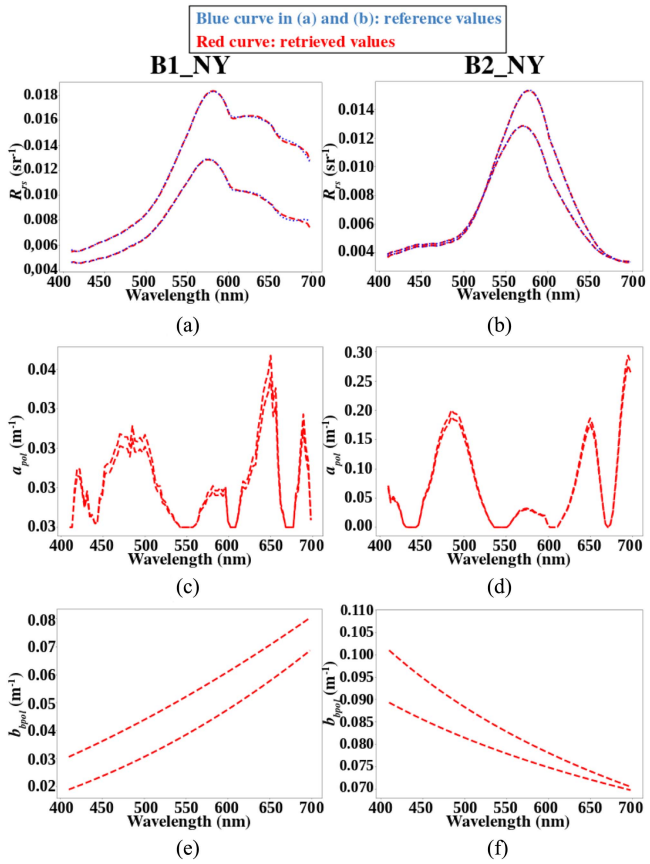

Fig. 10. R_{rs} and IOPs retrieved with IWOC algorithm applied to the airborne image of the zinc plant. (a) and (b) Spectral reflectance for B1-NY and B2-NY, respectively. (c) and (d) Absorption coefficient of the pollutant for B1-NY and B2-NY, respectively. (e) and (f) Backscattering coefficient of the pollutant for B1-NY and B2-NY, respectively.

coefficient b_{bpol} with wavelength with a maximum value of 0.08 m^{-1} [Fig. 10(e)]. B2-NY pond shows a decrease of b_{bpol} with wavelength with a maximum value of 0.10 m^{-1} [Fig. 10(f)]. Note that Mie calculations for this case also suggest that B1-NY may consist of larger particles than B2-NY (Section II-B). The a priori knowledge of the study area points out that B1-NY is used to settle muds [32], which is consistent with the occurrence of coarser particles (Section II-A).

2) Spatial Distribution of the Parameters: Fig. 11 shows the spatial variation of the retrieved parameters for B1-NY. The variations of C_{pol} are large, ranging from 0.0 to 2.0 [Fig. 11(a)]. Its average and standard deviation values are 0.71 and 0.26, respectively. The main variations in C_{pol} are observed in the center of the pond, where the values are around 1.2 and at the lower western tip of the pond, where the values are the highest. Such values may be the result of a discharge from the plant [green arrow in Fig. 11(a)].

The spatial variation of the depth suggests that the pond is shallow, with a maximum depth of 1 m [Fig. 11(b)]. The spatial features that are observed for the bottom morphology of B1-NY in the color image [Fig. 1(b)] are also observed on the distribution of H [(Fig. 11(b)].

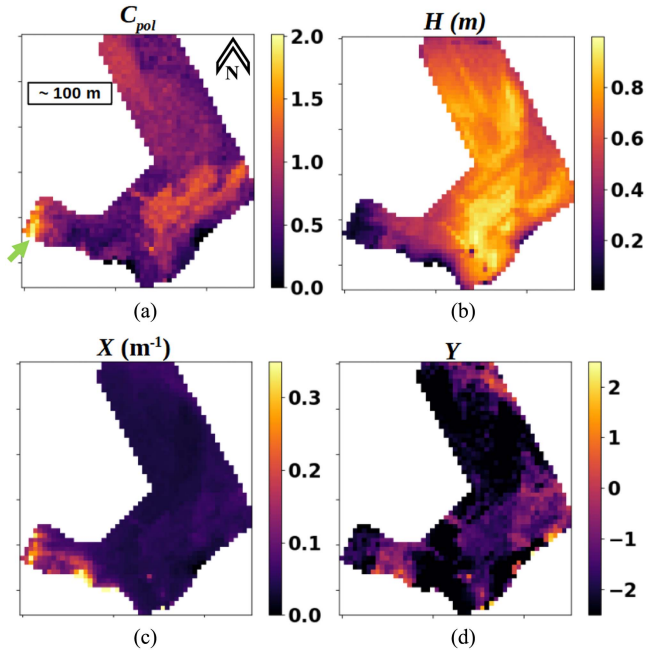

Fig. 11. Spatial distribution of retrieved IOPs parameters for pond B1-NY using the monopixel inversion: (a) C_{pol}, (b) H(m), (c) X(m^{-1}), and (d) Y. Green arrow is the supposed discharge location.

Pond B1-NY shows a weak mean value of 0.06 m^{-1} for X. A maximum value of 0.8 m^{-1} is observed for a single pixel at the southwest of the pond [Fig. 11(c)]. Low values of X mean that the pond contains weak amounts of suspended matter. Higher values are expectedly observed in the area where the effluent is assumed to be discharged into the pond [green arrow in Fig. 11(a)]. The retrieval of the spectral slope Y shows a more complex spatial distribution across the pond with a wide range of values, ranging from -2 to 2 [Fig. 11(d)]. The highest values are observed in the east corner of the pond, whereas the lowest values are in the western side. Fig. 12(a) shows the homogeneity of the pollutant across pond B2-NY with values of C_{pol} ranging from 1 to 1.5. Its mean value is 1.03 with a standard deviation of 0.08. The low standard deviation points out a homogeneous distribution with slightly higher values in the eastern half of the pond. The highest values of C_{pol} are observed at the northern tip of the pond and to a lower extent at the western tip. These high values are likely to be related with discharge locations [green arrows in Fig. 12(a)].

The estimation of the depth H seems to reach the upper limit (i.e., 10 m) for some pixels at the southern part of the pond, as a result of the significant absorption (i.e., dark color of the pond). Such area shows values as high as 10 m, whereas the mean value is 3.0 m with a relatively high standard deviation of 1.4 m. Out of all these pixels, the areas located in the northern and the western parts of the pond are the shallowest, whereas the southern part is the deepest area [(Fig. 12(b)]. The spatial distribution of X shows two areas with high values, which could be caused by releases of effluent [Fig. 12(c)]. These areas are located at the northern and western tips of the pond, which are consistent with observations of the spatial distribution of C_{pol}. The spatial distribution of the spectral slope of the backscattering coefficient Y reveals a

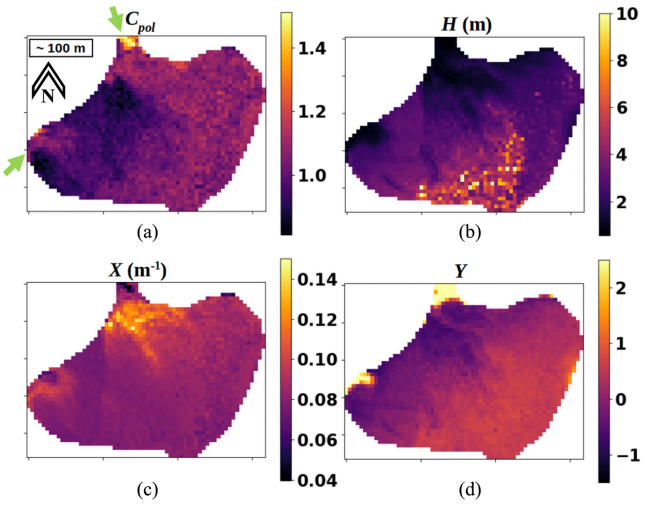

Fig. 12. Spatial distribution of retrieved IOPs parameters for pond B2-NY using the monopixel inversion: (a) $C_{\rm pol}$, (b) H(m), (c) $X(\mathrm{m}^{-1})$, and (d) Y. Green arrows are the supposed discharge locations.

plume [Fig. 1(b)] flowing from the north to the southeast part of the pond [Fig. 12(d)]. This flowing direction is consistent with the spatial variation of the depth: the water flows toward deeper parts of the pond. Note that the two areas where high values of $C_{\rm pol}$ and X were observed are also noticeable on the spatial distribution of Y.

In summary, the spatial variation of the overall retrieved parameters is informative on the pollutant's displacement through the pond. It is also informative on how its concentration could vary from its release at the upper and western regions of the pond to the southernmost point.

IV. Discussion

Previous methods to characterize polluted waters required in situ measurements for calibrating empirical models (e.g., [23], [24], [25]). The IWOC algorithm enables the optical characterization of diverse industrial ponds without specific calibration measurements. In addition, the IWOC method also allows analyzing the spatial distribution of the suspended matter and bottom depth. In [29], a pollutant optical contribution was introduced into the Lee model. In comparison to the model in [29], the IWOC method does not require a priori knowledge of the pollutant absorption coefficient for the initialization of its retrieval.

The water chemical composition homogeneity is a reliable assumption in industrial ponds. Assuming the factory follows the same industrial process, the plant's discharge remains chemically stable. In addition, the significant water pollution prevents the development of organisms [52], thereby reducing heterogeneity in the chemical composition. It is essential to note that this assumption may result in $R_{\rm rs}$ values showing the same spectral shapes. Therefore, it is crucial to select at least two $R_{\rm rs}$ with different magnitudes to enhance the effectiveness of the multipixel inversion.

For convenience, the value of the bottom reflectance is determined based on the image data. Only the parameter B is related to the bottom reflectance. Such an assumption remains valid when the entire bottom area of the pond is covered with the same material. As an example, the bottom of pond B2-NY is made of geotextile, which is mainly covered with goethite [Fig. 1(b) and personal communication]. Consequently, for convenience, it was assumed that the bottom reflectance $\rho_{\rm bottom}$ is goethite. However, goethite may not be present at some locations, which leads to a geotextile bottom reflectance instead. For the latter case, a different bottom reflectance value should be considered. In a case of highly turbid water, the selection of the value of the bottom reflectance is less crucial.

The evaluation of the performances of the IWOC algorithm on synthetic datasets, for which the IOPs are computed using Mie theory, points out potential tradeoffs between the absorption coefficient of natural constituents and the absorption and backscattering coefficients of a given pollutant. These tradeoffs are particularly pronounced when the additional pollutant absorption relates to the natural absorption signatures, such as the case of the IOPs of hematite outlined in Section III-A. For this latter case, it is worth noting that the spectral shape of the absorption coefficient of the pollutant $a_{\rm pol}$ shows similarities to that of the natural constituents (i.e., not polluted materials), particularly $a_{\rm CDOM}$. Parameter G was therefore overestimated during the monopixel initialization step, leading to an underestimation of $a_{\rm pol}$ at the next step [Fig. 13]. Tradeoffs may also arise between $a_{\rm pol}$ and $b_{\rm bpol}$ given their combined contribution. Various approaches could be used to mitigate this issue, such as a multiobjective minimization technique, which may enhance the performance of the retrieval toward a more realistic absorption coefficient.

The IWOC approach uses a local minimization algorithm. The primary issue is that it may cause ambiguity in the retrievals because of the likely occurrence of local minima. A large variety of random values have been tested for the initialization process. In this article, the IWOC algorithm is stable and seems to be independent of the initialization step. As a result, the algorithm is initialized by assuming a pure water component. For this initialization step, the initial values of P, G, X, and Y are set to zero, whereas B and H are assigned a value of 1.

The use of ATCOR may also cause uncertainties in $R_{\rm rs}$ data derived from airborne measurements over water bodies. ATCOR has been primarily designed to correct for atmospheric effects over land. Here, the atmospheric correction applied to the signal over water was interpolated using the surrounding land pixels.

The IWOC algorithm successfully retrieves $R_{\rm rs}$ from the airborne images. The derived IOPs values are in agreement with a priori knowledge of the study areas. The spatial variation of the retrieved parameters ($R_{\rm rs}$ and IOPs) showed some interesting features. The discharge locations for each pond could be identified using the spatial distribution of $C_{\rm pol}$ or X, which are informative as well on the flowing direction/displacement of the water. In addition, differences in the concentration of particulate matter between the various ponds could be monitored.

V. Conclusion

In this article, an original algorithm named IWOC has been developed to determine the IOPs of industrial wastewater ponds using imaging spectroscopy data. The main originalities of IWOC are the retrieval of the pollutant absorption coefficient $a_{\mathrm{pol},}$ backscattering coefficient $b_{\mathrm{bpol},}$ and its associated spectral slope Y without a priori information, for the first time to our knowledge. It was observed that Y could vary over positive and negative values, thus meaning that b_{bpol} may spectrally increase or decrease with wavelength as an indicator of the presence of coarse particles.

The IWOC algorithm is based on the semianalytical Lee model [30], which has been modified to take into account the absorption and backscattering coefficients of a pollutant (in addition to the natural water constituents). IWOC uses a multipixel alternating inversion technique to specifically retrieve the absorption properties (P and G), the backscattering parameters (X and Y), the bottom parameters (B and H), and the IOPs of the pollutant (C_{pol} and $a_{\mathrm{pol}}^{\mathrm{ref}}$). The retrieval of the remote sensing reflectance R_{rs} is satisfactory with values of RMSE ranging from close to zero for the synthetic datasets to a maximum value of 5.82×10^{-4} sr^{-1} for the airborne datasets. The retrieval of the IOPs of a given pollutant are also satisfactory for the synthetic datasets. The absorption signatures of the pollutant are retrieved with an RMSE value of 2.46×10^{-3} m^{-1} for dataset #1 (absorption-dominated scenario) and the backscattering coefficient with an RMSE close to zero for dataset #2 (backscattering-dominated scenario, Section III-A1). Dataset #3 and dataset #4 are allowed to evaluate IWOC on cases with more complex and realistic IOPs. This evaluation of the performances highlighted potential tradeoffs as well as model errors due to the defined spectral shape of the backscattering coefficient. A sensitivity analysis showed that noise in the data particularly affects the retrieval of the backscattering coefficient of the pollutant (Section III-A2). For the highest amount of noise, the errors (MAPE) values of Y range between 85% and 100% for dataset #2 and about 10 times more for dataset #1 (835% to 1083%).

This article demonstrates the feasibility of a generic inversion method for detecting polluted waters and retrieving the IOPs of the pollutants without the need of calibration data as for empirical and site-specific methods. Although a wide range of tests and evaluations of IWOC are carried out in this article (and some are still in progress), further investigations are needed to better evaluate its capabilities. As an example, a chemically oriented study should be carried out and a deeper analysis of the composition and optical properties of the dissolved/suspended matter should be continued with the goal of building a dedicated database to characterize industrial pollutants. Such a database would be relevant for the rapid, large-scale, and low-cost detection of pollution events in aquatic systems. Also, such investigations may provide insights to define the range of pollutant concentrations that the method could accurately measure.

The availability of a database could also be relevant for the development of supervised deep-learning algorithms for pollutant detection and identification. Reflectance databases of polluted waters could be helpful in the development of unsupervised deep-learning algorithms. The latter could be used in methods for feature extraction and classification of pollutant information from hyperspectral data of polluted waters. IWOC method could be integrated in such deep-learning process in direct or inverse mode. Furthermore, multimodal data fusion could provide more information on the pollutant, enhancing the accuracy and reliability of pollutant detection and identification. Real-time monitoring of pollutant levels and trends is crucial in the industrial wastewater treatment process to promptly implement corresponding control measures. Therefore, researchers are dedicated to developing real-time monitoring systems based on hyperspectral technology and integrating them with automation control techniques to achieve real-time regulation of the industrial wastewater treatment process. The approach conducted here is a first step toward a generic inversion method for the optical characterization of pollution sources in water in industrial ponds. Further article could lead to an operational method applicable to a wider range of water bodies.

Appendix

A. Mie Calculations

Mie theory can be used to calculate the IOPs for various ranges of particle types and size distributions. The Mie calculations code used here originates from [53] and has been ported to Python by Cornelius Dullemond from the Fortran77 code by Bruce Draine. The optical efficiency factors can be computed for a defined range of wavelengths, here 400–750 nm, and radius of different type of particles. These efficiency factors are then integrated throughout a defined particle size distribution (PSD) to calculate the IOPs, namely the absorption, scattering, backscattering, and extinction coefficients. The PSD used here consists of a combination of lognormal ($n_{\log}(r)$) and Junge power law ($n_{\mathrm{PL}}(r)$) distributions [54]. The total number of particles could then be expressed as $n_{\mathrm{total}}(r) = n_{\mathrm{PL}}(r) \times P_{\mathrm{PL}} + n_{\log}(r) \times P_{\log}$, where P_{PL} and $P_{\log}$ are the proportions of each type of size distribution, respectively. The use of such a mixture is supported by the fact that hydrosols in water, which usually follows a Junge power law distribution as a background [18], could show an additional mode of monodispersed particle size in industrial ponds as a result of discharges of a specific pollutant from the plant. The Junge power law distribution [54] is defined as

$$n_{\mathrm{PL}}(r) = \mathrm{const} \times \left(\frac{r}{r_0}\right)^{-\nu} \tag{A1}$$

where r is the radius, r_0 is a reference radius, and ν is the Junge exponent of the power law. The value of ν is typically 4 in natural waters [54] but it can vary from 2.5 to 6 [55], [56], [57]. Since the total number of particles, N (m^{-3}), is dependent on the concentration, the Junge distribution is normalized as follows:

$$\mathrm{const} = \frac{1-\nu}{r_0^{\nu}\left(r_{\max}^{1-\nu} - r_{\min}^{1-\nu}\right)} \tag{A2}$$

where $r_{\min}$ and $r_{\max}$ are the minimum and maximum radius of the size distribution, respectively.

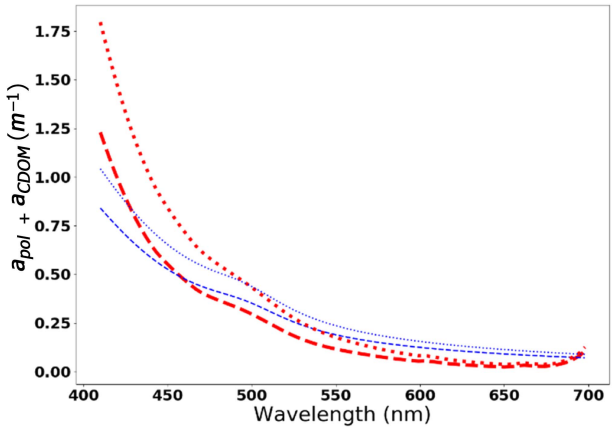

Fig. 13. Comparison between real (blue) and retrieved (red) values of $a_{\mathrm{pol}} + a_{\mathrm{CDOM}}$ for dataset #3 (Section III-A).

The lognormal distribution allows parameterizing the range of sizes of the dominant hydrosol, such as those that are released by the plant. The lognormal law is defined as

$$n_{\log}(r) = \frac{1}{\ln(\sigma)\, r\sqrt{2x\pi}} \times e^{-0.5\left(\frac{\ln(r)-\ln(r_m)}{\ln(\sigma)}\right)^2} \tag{A3}$$

where r_m is the modal radius of the center of the lognormal distribution. To take the concentration of particles (g/m^3) into account, the total number of log-normally distributed particles $N(r)$ is expressed as $N(r) = n_{\mathrm{total}}(r) \times N$, where N is defined based on the concentration such as follows:

$$N = \frac{3C_v}{4\pi \int_{r_{\min}}^{r_{\max}} r^3 n(r)\, dr} \tag{A4}$$

where C_v is the volume concentration (dimensionless).

B. Illustration of a Compensation Effect Between the Retrieved IOPs When Ignoring the Occurrence of a Given Pollutant

Tradeoffs between the retrieved natural and pollutant IOPs were observed during the evaluation of IWOC performances on synthetic datasets using the IOPs from Mie calculations. An example of these tradeoffs has been shown for the hematite case (dataset #3) in Section III-A2. The spectral shape of the absorption coefficient of hematite decreases with wavelength, such as what is typically observed for the spectral shape of a_{CDOM}. Therefore, a_{CDOM} is overestimated during the monopixel initialization to compensate for the lack of consideration of any pollutant absorption coefficient a_{pol} at this step. The overestimation of parameter G causes an underestimation of a_{pol}. The comparison between real and retrieved values of $a_{\mathrm{pol}} + a_{\mathrm{CDOM}}$ highlights the effect of the tradeoffs [Fig. 13]. Here, the RMSE value is 0.14 m^{-1}.

Acknowledgment

The authors would like to thank the LPG Nantes laboratory (Université de Nantes, France) for the acquisition of the HySpex airborne images, the industrial companies Novacarb and Nyrstar for welcoming us on their sites, authorizing the bio-optical data acquisition, and sharing the chemical analysis when available through personal communications. The authors are grateful to the Commissariat à l'énergie atomique et aux énergies alternatives (CEA, France) for funding the Ph.D. fellowship of Louis Zaugg and the field experiments.

References

[1] M. A. Caretta et al., *Water. In: Climate Change 2022: Impacts, Adaptation and Vulnerability. Contribution of Working Group II to the Sixth Assessment Report of the Intergovernmental Panel on Climate Change*. Cambridge, U.K.: Cambridge Univ. Press, 2022, pp. 551–712.

[2] R. Williams and L. Mink, "Settling ponds as a mining wastewater treatment facility. Pamphlet," *Idaho Bur. Mines Geol.*, vol. 164, pp. 1–41, 1975.

[3] M. Von Sperling, *Wastewater Characteristics, Treatment and Disposal*. London, U.K.: IWA Publishing, 2007.

[4] H. M. Dierssen et al., "Living up to the hype of hyperspectral aquatic remote sensing: Science, resources and outlook," *Front. Environ. Sci.*, vol. 9, 2021, Art. no. 649528.

[5] J. C. Ritchie, P. V. Zimba, and J. H. Everitt, "Remote sensing techniques to assess water quality," *Photogrammetric Eng. Remote Sens.*, vol. 69, no. 6, pp. 695–704, 2003.

[6] M. Bonansea, M. Ledesma, C. Rodriguez, and L. Pinotti, "Using new remote sensing satellites for assessing water quality in a reservoir," *Hydrol. Sci. J.*, vol. 64, no. 1, pp. 34–44, 2019.

[7] M. Elhag, I. Gitas, A. Othman, J. Bahrawi, and P. Gikas, "Assessment of water quality parameters using temporal remote sensing spectral reflectance in arid environments, Saudi Arabia," *Water*, vol. 11, no. 3, 2019, Art. no. 556.

[8] A. I. Flores-Anderson et al., "Hyperspectral satellite remote sensing of water quality in lake Atitlán, Guatemala," *Front. Environ. Sci.*, vol. 8, 2020, Art. no. 7.

[9] C. Mobley, D. Stramski, W. Paul Bissett, and E. Boss, "Optical modeling of ocean waters: Is the case 1–case 2 classification still useful?," *Oceanography*, vol. 17, no. 2, pp. 60–67, 2005.

[10] H. R. Gordon and A. Y. Morel, in *Remote Assessment of Ocean Color for Interpretation of Satellite Visible Imagery: A Review*. New York: Springer-Verlag, 1983. [Online]. Available: https://doi.org/10.1029/LN004

[11] A. Morel and B. Gentili, "A simple band ratio technique to quantify the colored dissolved and detrital organic material from ocean color remotely sensed data," *Remote Sens. Environ.*, vol. 113, no. 5, pp. 998–1011, 2009.

[12] B. Lubac, H. Loisel, N. Guiselin, R. Astoreca, L. F. Artigas, and X. Mériaux, "Hyperspectral and multispectral ocean color inversions to detect phaeocystis globosa blooms in coastal waters," *J. Geophys. Res.*, vol. 113, no. C06026, 2008, pp. 1–17, doi: 10.1029/2007JC004451.

[13] E. Torrecilla, D. Stramski, R. A. Reynolds, E. Millán-Núñez, and J. Piera, "Cluster analysis of hyperspectral optical data for discriminating phytoplankton pigment assemblages in the open ocean," *Remote Sens. Environ.*, vol. 115, no. 10, pp. 2578–2593, 2011.

[14] R. W. Preisendorfer, C. D. Mobley, and T. P. Barnett, "The principal discriminant method of prediction: Theory and evaluation," *J. Geophys. Res.: Atmos.*, vol. 93, no. D9, pp. 10815–10830, 1988.

[15] R. N. Clark and T. L. Roush, "Reflectance spectroscopy: Quantitative analysis techniques for remote sensing applications," *J. Geophys. Res.: Solid Earth*, vol. 89, no. B7, pp. 6329–6340, 1984.

[16] C. Mobley, *Light and Water: Radiative Transfer in Natural Waters*. New York, NY, USA: Academic Press, 1994.

[17] M. Chami, B. Lafrance, B. Fougnie, J. Chowdhary, T. Harmel, and F. Waquet, "OSOAA: A vector radiative transfer model of coupled atmosphere-ocean system for a rough sea surface application to the estimates of the directional variations of the water leaving reflectance to better process multi-angular satellite sensors data over the ocean," *Opt. Exp.*, vol. 23, no. 21, pp. 27829–27852, 2015.

[18] P. Gege, "The water color simulator WASI: An integrating software tool for analysis and simulation of optical in situ spectra," *Comput. Geosci.*, vol. 30, no. 5, pp. 523–532, 2004.

[19] Z. Lee, K. L. Carder, C. D. Mobley, R. G. Steward, and J. S. Patch, "Hyperspectral remote sensing for shallow waters. I. A semianalytical model," *Appl. Opt.*, vol. 37, no. 27, pp. 6329–6338, 1998.

[20] S. B. Kotsiantis, I. D. Zaharakis, and P. E. Pintelas, "Machine learning: A review of classification and combining techniques," *Artif. Intell. Rev.*, vol. 26, pp. 159–190, 2006.

[21] A. Plaza et al., "Recent advances in techniques for hyperspectral image processing," *Remote Sens. Environ.*, vol. 113, pp. S110–S122, 2009.

[22] M. Paoletti, J. Haut, J. Plaza, and A. Plaza, "Deep learning classifiers for hyperspectral imaging: A review," *ISPRS J. Photogrammetry Remote Sens.*, vol. 158, pp. 279–317, 2019.
[23] S. Kar et al., "Classification of river water pollution using hyperion data," *J. Hydrol.*, vol. 537, pp. 221–233, 2016.
[24] J. Dai, D. Wang, R. Wang, and Z. Chen, "Quantitative estimation of concentrations of dissolved rare earth elements using reflectance spectroscopy," *J. Appl. Remote Sens.*, vol. 7, no. 1, 2013, Art. no. 073513.
[25] E. Choe, F. van der Meer, F. van Ruitenbeek, H. van der Werff, B. de Smeth, and K.-W. Kim, "Mapping of heavy metal pollution in stream sediments using combined geochemistry, field spectroscopy, and hyperspectral remote sensing: A case study of the Rodalquilar mining area, SE Spain," *Remote Sens. Environ.*, vol. 112, no. 7, pp. 3222–3233, 2008.
[26] L. Goddijn-Murphy, S. Peters, E. Van Sebille, N. A. James, and S. Gibb, "Concept for a hyperspectral remote sensing algorithm for floating marine macro plastics," *Mar. Pollut. Bull.*, vol. 126, pp. 255–262, 2018.
[27] K. Haule, M. Darecki, and H. Toczek, "Light penetration in seawater polluted by dispersed oil: Results of radiative transfer modelling," *J. Eur. Opt. Soc.-Rapid Pub.*, vol. 10, 2015, Art. No. 15052
[28] S. Hafee et al., "Detection and monitoring of marine pollution using remote sensing technologies," Monitoring of Marine Pollution. IntechOpen, Jun. 2019, doi: 10.5772/intechopen.81657.
[29] R. Deng, S. Xiong, and Y. Qin, "Water pollution remote sensing for pearl river delta," in *Proc. Geoinform. Joint Conf. GIS Built Environ.: Monit. Assessment Natural Resour. Environ.*, 2008, pp. 827–834.
[30] Z. Lee, K. L. Carder, C. D. Mobley, R. G. Steward, and J. S. Patch, "Hyperspectral remote sensing for shallow waters: 2. deriving bottom depths and water properties by optimization," *Appl. Opt.*, vol. 38, no. 18, pp. 3831–3843, 1999.
[31] Nyrstar Corporate Office. *Nyrstar Auby metals processing*. Accessed: Mar. 1, 2024. [Online]. Available: https://www.nyrstar.com/operations/metals-processing/nyrstar-auby
[32] Direction Régionale de l'Environnement de l'Aménagement et du Logement Grand Est. *Rapport de l'Inspection des installations classées*. Apr. 2023. [Online]. Available: https://georisques.gouv.fr/webappReport/ws/installations/inspection/QstT0aYMBLetTqq1YG5GyclYkIE9z1j6
[33] S. Edelblutte, "'Les montagnes qui poussent' ou l'impact des rejets salins des soudières de l'agglomération nancéienne /the 'mountains which rise up' or the impact on the landscape of salt effluents from the soda works of the urban area of Nancy," *Revue de Géographie de Lyon*, vol. 74, no. 3, pp. 243–251, 1999.
[34] Direction Régionale de l'Environnement de l'Aménagement et du Logement des Hauts-de-France, *Rapport de l'Inspection des installations classées*, Jul. 2022. [Online]. Available: https://georisques.gouv.fr/webappReport/ws/installations/inspection/ctFqwjw8a1G3R3kvHTSMCxri7r0t2XYo
[35] R. Richter and D. Schläpfer, "Geo-atmospheric processing of airborne imaging spectrometry data. Part 2: Atmospheric/topographic correction," *Int. J. Remote Sens.*, vol. 23, no. 13, pp. 2631–2649, 2002.
[36] S. Maritorena, A. Morel, and B. Gentili, "Diffuse reflectance of oceanic shallow waters: Influence of water depth and bottom albedo," *Limnol. Oceanogr.*, vol. 39, no. 7, pp. 1689–1703, 1994.
[37] R. M. Pope and E. S. Fry, "Absorption spectrum (380–700 nm) of pure water. II. Integrating cavity measurements," *Appl. Opt.*, vol. 36, no. 33, pp. 8710–8723, 1997.
[38] L. Kou, D. Labrie, and P. Chylek, "Refractive indices of water and ice in the 0.65-to 2.5-μm spectral range," *Appl. Opt.*, vol. 32, no. 19, pp. 3531–3540, 1993.
[39] Z. Lee, K. L. Carder, S. K. Hawes, R. G. Steward, T. G. Peacock, and C. O. Davis, "Model for the interpretation of hyperspectral remote-sensing reflectance," *Appl. Opt.*, vol. 33, no. 24, pp. 5721–5732, 1994.
[40] A. Bricaud et al., "Absorption by dissolved organic matter of the sea (yellow substance) in the UV and visible domains," *Limnol. Oceanogr.*, vol. 26, no. 1, pp. 43–53, 1981.
[41] K. L. Carder, S. Hawes, K. Baker, R. Smith, R. Steward, and B. Mitchell, "Reflectance model for quantifying chlorophyll a in the presence of productivity degradation products," *J. Geophys. Res.: Oceans*, vol. 96, no. C11, pp. 20599–20611, 1991.
[42] R. C. Smith and K. S. Baker, "Optical properties of the clearest natural waters (200–800 nm)," *Appl. Opt.*, vol. 20, no. 2, pp. 177–184, 1981.
[43] Z. Lee, K. L. Carder, and R. A. Arnone, "Deriving inherent optical properties from water color: A multiband quasi-analytical algorithm for optically deep waters," *Appl. Opt.*, vol. 41, no. 27, pp. 5755–5772, 2002.
[44] G. Mie, "Sättigungsstrom und stromkurve einer schlecht leitendenflüssigkeit," *Annalen der Physik*, vol. 331, no. 8, pp. 597–614, 1908.
[45] T. S. Kostadinov, D. A. Siegel, and S. Maritorena, "Retrieval of the particle size distribution from satellite ocean color observations," *J. Geophys. Res.*, vol. 114, no. C09015, pp. 1–22, 2009, doi: 10.1029/2009JC005303.
[46] C. B. Markwardt, "Non-linear least squares fitting in IDL with MPFIT," in *Proceedings of Astronomical Data Analysis Software and Systems XVIII, Quebec, Canada, ASP Conference Series*, vol. 411, D. Bohlender, P. Dowler, and D. Durand, Eds. San Francisco, CA, USA: Astronomical Society of the Pacific, 2009, pp. 251–254.
[47] J. C. Bezdek and R. J. Hathaway, "Convergence of alternating optimization," *Neural, Parallel Sci. Comput.*, vol. 11, no. 4, pp. 351–368, 2003.
[48] J. Dai, D. Wang, and Z. Chen, "Dissolved rare earth elements estimation of ion-absorption rare earth ores using reflectance spectroscopy in south Jiangxi province, China," *J. Rare Earths*, vol. 39, no. 10, pp. 1300–1310, 2021.
[49] X. L. Zhang, G. J. Wu, C. L. Zhang, T. L. Xu, and Q. Q. Zhou, "What is the real role of iron oxides in the optical properties of dust aerosols?," *Atmos. Chem. Phys.*, vol. 15, pp. 12159–12177, 2015.
[50] C. Ye, E. C. Sklute, and T. D. Glotch, "Orientation averaged visible/nearinfrared and mid-infrared optical constants of hydrous Ca-sulfates: Gypsum and bassanite," *Earth Space Sci.*, vol. 8, no. 10, 2021, Art. no. e2021EA001834.
[51] A. H. M. J. Triaud, Private Communication, 2005. [Online]. Available: https://eodg.atm.ox.ac.uk/ARIA/data
[52] P. M. D'Costa, M. S. D'Silva, and R. K. Naik, "Impact of pollution on phytoplankton and implications for marine econiches," in *Marine Pollution and Microbial Remediation*, M. Naik and S. Dubey, Eds. Berlin, Germany: Springer, 2017.
[53] C. F. Bohren and D. R. Huffman, *Absorption Scattering Light by Small Particles*. Hoboken, NJ, USA: Wiley, 2008.
[54] C. Junge, "The size distribution and aging of natural aerosols as determined from electrical and optical data on the atmosphere," *J. Atmos. Sci.*, vol. 12, pp. 13–25, Feb. 1955.
[55] D. Risovic, "Two-component model of sea particle size distribution," *Deep Sea Res. Part I: Oceanogr. Res. Papers*, vol. 40, no. 7, pp. 1459–1473, 1993.
[56] E. Boss, M. S. Twardowski, and S. Herring, "Shape of the particulate beam attenuation spectrum and its inversion to obtain the shape of the particulate size distribution," *Appl. Opt.*, vol. 40, pp. 4885–4893, Sep. 2001.
[57] H. Loisel, J.-M. Nicolas, A. Sciandra, D. Stramski, and A. Poteau, "Spectral dependency of optical backscattering by marine particles from satellite remote sensing of the global ocean," *J. Geophys. Res.*, vol. 111, no. C09024, pp. 1–14, 2006, doi: 10.1029/2005JC003367.

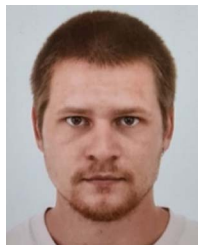

Louis Zaugg was born in Singapour, in 1997. He received the M.Sc. degree in planetology from the Sorbonne University, Paris, France, in 2020. He is currently working toward the Ph.D. degree in signal and image processing with the French Atomic Energy and Alternative Energies Commission (CEA), the Optics Department, French Aerospace Laboratory (ONERA), Sorbonne University.

His research interests include image and signal processing as well as new methodological developments for hyperspectral imagery.

Rodolphe Marion was born in Paris, France, in 1976. He received the Ing. degree in electronics engineering from the Ecole Nationale Supérieure de l'Electronique et de ses Applications, Cergy-Pontoise, France, in 2000, the Ph.D. degree in image processing from the University of Cergy-Pontoise, Cergy-Pontoise, France, in 2003, and the Habilitation à Diriger des Recherches in hyperspectral remote sensing from the University Pierre et Marie Curie, Paris, France, in 2016.

He is currently a Research Director with the French Atomic Energy and Alternative Energies Commission. He does research in hyperspectral remote sensing applied to the characterization of industrial environments. His research interests include detection and quantification of gas and aerosol plumes, the identification of industrial minerals, and the characterization of industrial wastewater. His research interests also include digital image and signal processing as well as new methodological developments in hyperspectral imaging.

Malik Chami received the Ph.D. degree in coastal waters remote sensing from the Université du Littoral Côted'Opale, France, in 1997.

He is currently a Professor in physics with the Sorbonne Université and with the Laboratoire Lagrange (Observatoire Côte d'Azur) (France). He works on ocean color remote sensing for the detection of suspended matter from satellite sensors. He is an expert on radiative transfer modeling for the coupled atmosphere–ocean system. He contributed to develop inverse methods for retrieving the bio-optical properties of hydrosols. He is also involved in the development of optical instrumentation.

Xavier Briottet received the Ph.D. degree in electronics from the Ecole Nationale Supérieure de l'Aéronautique et de l'Espace, Toulouse, France, in 1986, and the "Habilitation à Diriger des Recherches" in remote sensing from the Université Paul Sabatier, Toulouse, France, in 1999.

In 1987, he became an Assistant Professor of signal and image processing with the Ecole Supérieure d'Electricité, Gif-sur-Yvette, France. Since 1988, he has been working on remote sensing with the Optics Department, French Aerospace Laboratory (ONERA), Toulouse, France. He is currently a Research Director and an Adviser of the active and passive optical remote sensing. He is currently a PI of a future hyperspectral space mission with the French Space Agency (CNES). His research interests include 3-D radiative transfer in urban areas, shadow detection, anthropic aerosol characterization, unmixing in the reflective and thermal domains, and using high spatial hyperspectral imagery.

Laure Roupioz received the Ph.D. degree in remote sensing from Delft University of Technology, The Netherlands, and the Université de Strasbourg, France, in 2015.

She is currently a Senior Scientist with the Optics Department, ONERA, Toulouse, France. She is an experienced Researcher in Earth observation applications ranging from land surface reflectance and temperature retrieval over heterogeneous and complex terrain to oil spill detection studies. She has a solid track record in the estimation of optical properties from remote sensing multi and hyperspectral data covering the shortwave to the thermal domain. She is also involved in the preparation of future infrared satellite missions.